PHYSICAL REVIEW E **93**, 023116 (2016)

# Flow-induced compaction of a deformable porous medium

Duncan R. Hewitt,[1,2] Japinder S. Nijjer,[1,3] M. Grae Worster,[1] and Jerome A. Neufeld[1,4,5]
[1]*Department of Applied Mathematics and Theoretical Physics, University of Cambridge, Cambridge CB3 0WA, United Kingdom*
[2]*Department of Mathematics, University of British Columbia, Vancouver, V6T 1Z2, Canada*
[3]*Department of Engineering Science, University of Toronto, Toronto, M5S 2E4, Canada*
[4]*Department of Earth Sciences, University of Cambridge, Cambridge CB3 0EZ, United Kingdom*
[5]*BP Institute, University of Cambridge, Cambridge CB3 0EZ, United Kingdom*
(Received 24 June 2015; revised manuscript received 1 January 2016; published 24 February 2016)

Fluid flowing through a deformable porous medium imparts viscous drag on the solid matrix, causing it to deform. This effect is investigated theoretically and experimentally in a one-dimensional configuration. The experiments consist of the downwards flow of water through a saturated pack of small, soft, hydrogel spheres, driven by a pressure head that can be increased or decreased. As the pressure head is increased, the effective permeability of the medium decreases and, in contrast to flow through a rigid medium, the flux of water is found to increase towards a finite upper bound such that it becomes insensitive to changes in the pressure head. Measurements of the internal deformation, extracted by particle tracking, show that the medium compacts differentially, with the porosity being lower at the base than at the upper free surface. A general theoretical model is derived, and the predictions of the model give good agreement with experimental measurements from a series of experiments in which the applied pressure head is sequentially increased. However, contrary to theory, all the experimental results display a distinct and repeatable hysteresis: the flux through the material for a particular applied pressure drop is appreciably lower when the pressure has been decreased to that value compared to when it has been increased to the same value.

DOI: 10.1103/PhysRevE.93.023116

## I. INTRODUCTION

Deformation of a fluid-filled porous medium induces fluid flow through the medium, as can readily be observed in daily life by squeezing out a kitchen sponge or walking on wet sand. Conversely, the flow of fluid through a medium exerts viscous shear stresses on the solid matrix and induces deformation. The study of coupled fluid flow and solid deformation is the basis of the theory of poro-elasticity (see, e.g., Refs. [1,2]), and continuing interest in the subject has, in part, been spurred by industrial applications to enhanced oil recovery, carbon dioxide sequestration and hydraulic fracturing. Poro-elastic behavior also underlies a number of open questions in geophysics, including the degree to which earthquake-induced deformation can drive long-lasting changes in crustal permeability (e.g., Refs. [3,4]) or provide a trigger for liquefaction or eruptions [5]. Despite a long history of study, simple table-top experimental methods for studying poro-elastic effects are rare. In this paper, we present an experimental study of one-dimensional compaction of a deformable medium driven by the flow of fluid through the medium, and compare the results with the predictions of a general two-phase theoretical model.

One-dimensional compaction of a two-phase mixture has been widely studied in a variety of settings beyond the realm of classical poro-elasticity. In a geophysical context, one-dimensional compaction problems have been investigated to describe gravitational compaction of sedimentary basins [6,7]. Industrial interest in the problem typically stems from the desire to "dewater" or reduce the liquid fraction of a suspension, with applications including disposal of waste mining slurries [8], treatment of waste water and sludge [9], compression of pulp fibers in the paper-making process [10], and compression of digesta in the intestine [11]. Although sedimentation under gravity is considered in some of these contexts [12], compaction and dewatering are more typically achieved by the application of a large external load to the mixture. This mechanism, known as "pressure filtration," is also often exploited as a means for bulk rheometry of multiphase suspensions [13,14].

While compaction due to the application of an external load has been fairly widely studied, previous investigations of flow-induced deformation are scarce. A simple and effective demonstration of the difference between these two cases was given by Parker *et al.* [15], who showed that the strain in a wet sponge is uniform under the application of an external mechanical load but varies with depth when fluid flows vertically through the sponge. A similar observation was later made by Lanir *et al.* [16]. The physical basis for this difference is that an external load results in a uniform stress throughout the medium, whereas the pressure gradients that drive fluid flow inevitably induce gradients in the stress, such that the load is distributed through the medium. On a practical level, one implication of differential, flow-induced compaction is that direct measurement of permeability as a function of porosity is not straightforward in deformable media. More recent experimental work in this area has considered flow-induced compaction in different geometries. For example, MacMinn *et al.* [17] presented an experimental study of pressure-driven fluid injection into a monolayer of elastic particles, and Nordstrom *et al.* [18] investigated compaction of similar particles in a centrifuge.

Our goal in this study is to provide a more thorough and quantitative exploration of the qualitative observations of flow-induced compression made by Parker *et al.* [15]. To this end, we report on a set of experiments to measure flow-induced, one-dimensional compression of a simple poro-elastic medium, and compare our results with the predictions of a new theoretical model. Our experimental setup consists of a saturated, deformable porous medium that is open to the atmosphere at its base. For a fixed pressure head, fluid flows down through the medium under gravity, causing the medium to compress. We measure the flow rate and change in depth of the medium. We take measurements for different pressure heads, and highlight the dependence of the deformation and flow on the stress history of the medium. In some experiments, we also measure the internal deformation through the medium by tracking a representative sample of individual particles.

Following various recent experiments [17–19], we used small polyacrylamide hydrogel particles to form a convenient deformable medium. As well as being straightforward to prepare and relatively inexpensive, these hydrogels are soft and elastic, which means that appreciable deformation can be obtained at fluid pressures that are readily achieved in the laboratory. The hydrogels are transparent, which allows for particle tracking and direct measurement of deformation in the medium, and they have a density that is very close to that of water, which removes any effects of gravitational compaction. Our theoretical model follows two-phase theory [20]; related formulations for different flow configurations can be found in many previous studies, e.g. Refs. [6,18,21–23]. Modeling of large-deformation poro-elasticity is discussed in detail in very recent work by MacMinn *et al.* [24].

The paper is laid out as follows. In Sec. II we present our general, two-phase model to describe one-dimensional, flow-driven compaction and discuss some of the features of the model. In Sec. III we describe the experimental setup, present the results, and compare them with the predictions of the model. In Sec. IV we discuss the results of this work.

## II. THEORETICAL MODELING

In this section we present a general theoretical framework to model flow-induced deformation in a one-dimensional system and discuss the qualitative predictions of the model for a specific choice of constitutive functions. This modeling sets the scene for our laboratory experiments, which are presented in Sec. III.

Consider a deformable porous medium of initial depth $l_0$ (in the absence of flow) and density $\rho$ in a rigid container. The medium is initially unstrained, and is fully saturated with and overlain by fluid, also of density $\rho$, up to a constant total depth $H$ above the base of the container [Fig. 1(a)]. The solid medium is held in place at the base of the container by a permeable mesh that can be opened to the atmosphere to allow fluid to flow through freely. When the base is opened, fluid flows down through the medium with a vertical Darcy flux $Q(t) \leq 0$ per unit cross-sectional area. The fluid exerts a viscous stress on the medium, causing it to compact to a depth $l(t) \leq l_0$ [Fig. 1(b)]. The constant depth $H$ of the fluid layer above the base of the medium is maintained by an external source of fluid.

### A. General model

We treat the individual solid and fluid phases as incompressible. Conservation of mass in each phase, Darcy's law, and stress balance therefore give

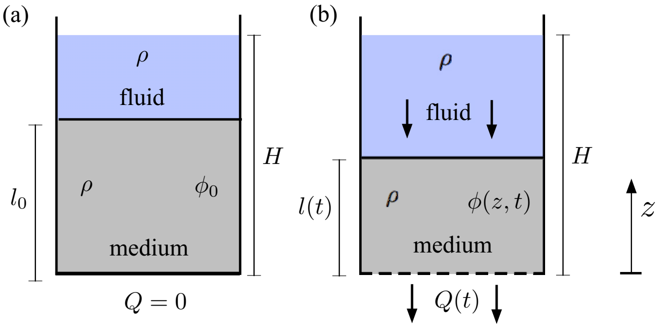

FIG. 1. The setup, with (a) an impermeable base and no flow, and (b) a base that is permeable to the fluid, but not the solid, and a downwards fluid flow with flux $Q(t)$ per unit area.

$$\frac{\partial \phi}{\partial t} + \frac{\partial}{\partial z}(\phi w_f) = 0, \tag{1a}$$

$$\frac{\partial}{\partial t}(1-\phi) + \frac{\partial}{\partial z}[(1-\phi)w_s] = 0, \tag{1b}$$

$$\phi(w_f - w_s) = -\frac{k}{\mu}\left(\frac{\partial p}{\partial z} + \rho g\right), \tag{1c}$$

$$\frac{\partial P}{\partial z} + \rho g = 0, \tag{1d}$$

where $w_f$ and $w_s$ are the fluid and solid velocities in the positive $z$ direction, $\phi$ is the porosity or liquid volume fraction, $k(\phi)$ is the permeability, which is assumed to remain isotropic, $\mu$ is the fluid viscosity, $g$ is the gravitational acceleration, $P$ is the total thermodynamic pressure, and $p$ is the fluid (pore) pressure. In other words, $P$ is the total force per unit area on the two-phase mixture, while $p$ is the local pressure in the fluid phase. We further define the *matrix pressure* $\sigma \equiv P - p$ to be the difference between the total and pore pressures, which is the overpressure on the matrix ($\sigma$ is equivalent to the osmotic pressure for colloidal suspensions; e.g., Ref. [25]). Following Terzaghi's principle in soil mechanics, the matrix pressure is assumed to satisfy a general elastic constitutive law $\sigma = \sigma(e)$, where $e$ is the linear strain of the system. Given that the deformation is constrained to be one-dimensional, the strain is related to the porosity by

$$e = \frac{\phi - \Phi}{1-\phi}, \tag{2}$$

by conservation of mass, where $\Phi$ is the uniform porosity that corresponds to zero strain on the matrix. The strain, and thus the porosity, are also related to the vertical displacement $\zeta(z)$ by

$$\frac{\partial \zeta}{\partial z} = 1 - \frac{1}{1+e} \Rightarrow \zeta(z) = \int_0^z \frac{\phi(z') - \Phi}{1-\Phi}\, dz'. \tag{3}$$

At the upper boundary of the medium, the total pressure and the pore pressure are equal and given by the hydrostatic head of the overlying fluid, such that $P(z = l) = p(z = l) = \rho g(H - l)$. At the open lower boundary, the pore pressure is atmospheric, which we scale to be zero. In terms of $\sigma$, these conditions reduce to

$$\sigma(z=0)=\rho g H, \quad \sigma(z=l)=0. \tag{4a,b}$$

The boundary conditions for the solid velocity are

$$w_s(z=0)=0, \quad w_s(z=l)=\frac{\partial l}{\partial t}, \tag{5a,b}$$

and the total fluid flux (in the positive $z$ direction) through the medium per unit cross-sectional area at any height is uniform and given by $Q(t)=(\phi\, w_f)|_{z=0}\leq 0$.

#### 1. Nondimensionalization

The model outlined above can be solved by the specification of constitutive laws for the matrix pressure $\sigma$ and the permeability $k$. In this work we restrict attention to functions of the form $\sigma(e(\phi))$ and $k(\phi)$, although we note that, in general, these properties may depend on the pore geometry as well as the porosity. Given these constitutive laws, which determine characteristic dimensional scales for the elastic modulus $\sigma^*$ and permeability $k^*$ of the matrix, we define dimensionless variables by scaling lengths with $l_0$, pressures with $\sigma^*$, permeability with $k^*$, velocity with $k^*\sigma^*/l_0\mu$, and time with $l_0^2\mu/k^*\sigma^*$. For example, the scales $\sigma^*$ and $k^*$ for a specific choice of $\sigma$ and $k$ are given in (15) below. We identify the dimensionless group

$$\mathcal{H}=\frac{\rho g H}{\sigma^*} \tag{6}$$

as a measure of the applied fluid pressure difference relative to the elastic modulus of the matrix.

Working in dimensionless variables, the continuity equations (1a) and (1b) can be combined and integrated to give

$$\phi w_f+(1-\phi)w_s=Q, \quad \Rightarrow \phi\big(w_f-w_s\big)=Q-w_s, \tag{7}$$

such that (1c) and (1d) reduce to

$$Q-w_s=k\frac{\partial\sigma}{\partial z}=k\sigma'\frac{\partial\phi}{\partial z}, \tag{8}$$

where $\sigma'=\partial\sigma/\partial\phi$. Back-substitution into (1b) gives a nonlinear advection-diffusion equation

$$\frac{\partial\phi}{\partial t}+Q\frac{\partial\phi}{\partial z}=-\frac{\partial}{\partial z}\left[(1-\phi)k\sigma'\frac{\partial\phi}{\partial z}\right], \tag{9}$$

with boundary conditions from (4),

$$\phi(0,t)=\phi_0(\mathcal{H}), \quad \phi[l(t),t]=\Phi, \tag{10a,b}$$

where $\phi_0$ is determined by the requirement that $\sigma(\phi_0)=\mathcal{H}$. The flux $Q$ and depth $l$ are determined from (5),

$$Q=k(\phi_0)\sigma'(\phi_0)\left.\frac{\partial\phi}{\partial z}\right|_{z=0}, \quad Q-\frac{\partial l}{\partial t}=k(\Phi)\sigma'(\Phi)\left.\frac{\partial\phi}{\partial z}\right|_{z=l}. \tag{11a,b}$$

Note that, unlike for a medium compressed by an external load, the porosity at the upper surface is fixed at its initial value (10b) because the pore pressure and total pressure are equal there.

#### 2. Steady states

In a steady state, the viscous stresses exerted by the fluid are balanced by compaction of the matrix, and the solid velocity $w_s$ is zero. Steady solutions are given by (8), together with dimensionless conservation of the solid phase,

$$\int_0^l(1-\phi)\,dz=(1-\Phi), \tag{12}$$

which can be converted into an integral over $\phi$ using (8). Equations (12) and the integral of (8) then yield expressions for the steady-state flux $Q_s$ and the depth $l_s$ of the medium:

$$Q_s=\int_{\phi_0}^{\Phi}\frac{(1-\phi)k(\phi)\sigma'(\phi)}{(1-\Phi)}\,d\phi, \tag{13a}$$

$$Q_s l_s=\int_{\phi_0}^{\Phi}k(\phi)\sigma'(\phi)\,d\phi. \tag{13b}$$

A practical measure of the steady-state resistance of the medium is provided by the "effective permeability" $k_{\text{eff}}=l[\int_0^l 1/k\,dz]^{-1}$, which is the ratio of the flow to the average pressure gradient such that

$$Q_s=-k_{\text{eff}}\frac{\mathcal{H}}{l_s}. \tag{14}$$

In the Appendix, we consider the possible behavior of the steady-state flux $Q_s$ for arbitrary constitutive functions $\sigma$ and $k$ in the asymptotic limit of very large applied pressure $\mathcal{H}\to\infty$.

### B. Specific model

In this section we consider a simple specific choice of the constitutive functions $\sigma(e(\phi))$ and $k(\phi)$ that will be appropriate for modeling the experimental setup, discussed in Sec. III. The experimental medium is composed of small elastic hydrogel particles. Under the assumption that the medium cannot be compacted beyond a limiting finite strain $e_m$, which corresponds to a minimum porosity $\phi_m$ from (2), and that the compacted medium is impermeable in this limit, we take simple constitutive laws for the dimensional matrix pressure and permeability of the form

$$\frac{\sigma}{\sigma^*}=-\frac{e}{1-e/e_m}, \quad \frac{k}{k^*}=\frac{(\phi-\phi_m)^3}{(1-\phi)^2}, \tag{15a,b}$$

where $\sigma^*$ is the elastic modulus of the saturated particles. Equation (15a) gives linear elastic behavior for small strains but diverges as $e\to e_m$. A similar relationship was used by Nordstrom *et al.* [18], who also discuss other possible rheological models for hydrogel particles. Equation (15b) is a generalized Kozeny-Carman permeability function for spherical packing, with $k^*=(r^2/45)\Phi^3/(\Phi-\phi_m)^3$, where $r$ is the average radius of the unstressed particles. We note that, in general, the behavior of $k(\phi)$ as $\phi\to\phi_m$ will depend on the flow geometry around the highly deformed particles in this limit and may be more complex than this simple assumed form.

For simplicity, for the remainder of this paper we set $\phi_m=0$, which gives $e_m=-\Phi$ from (2). The stress is therefore given

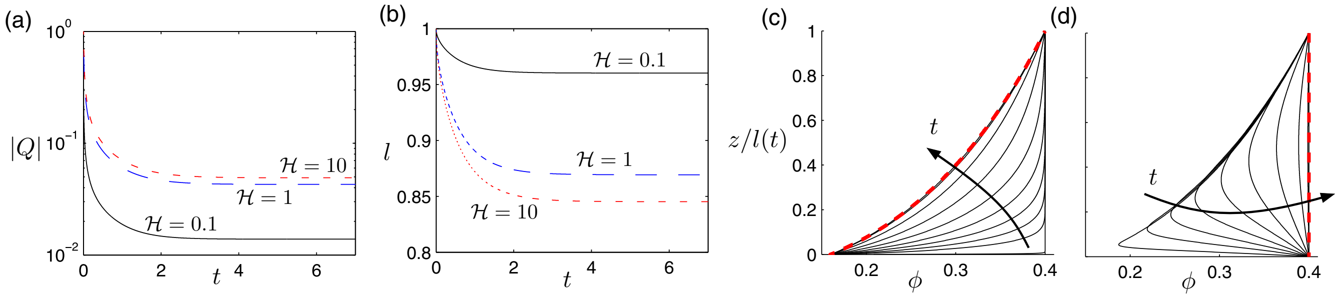

FIG. 2. Evolution to the steady state for a step change in the dimensionless fluid pressure difference $\mathcal{H}$. (a–b) Step increase at $t = 0$ from $\mathcal{H} = 0$ to $\mathcal{H} = 0.1$ (black solid), $\mathcal{H} = 1$ (blue long dashed), or $\mathcal{H} = 10$ (red short dashed): (a) the magnitude of the flux, and (b) the depth of the medium. (c–d) The porosity at times between $t = 0.01$ and $t = 5.12$, separated by a factor of 2, together with the steady-state solution from (23) (dashed), for (c) a step increase from $\mathcal{H} = 0$ to $\mathcal{H} = 1$, and (d) a step decrease from $\mathcal{H} = 1$ to $\mathcal{H} = 0$, starting from the steady-state solution of (c). All solutions have $\Phi = 0.4$.

in dimensionless form as a function of $\phi$ by

$$\sigma = \frac{\Phi}{1-\Phi}\left(\frac{\Phi-\phi}{\phi}\right). \tag{16}$$

### 1. Time-dependent theory

For the specific constitutive functions in (15) with $\phi_m = 0$, (9) is

$$\frac{\partial\phi}{\partial t} + Q\frac{\partial\phi}{\partial z} = \frac{\Phi^2}{(1-\Phi)}\frac{\partial}{\partial z}\left[\frac{\phi}{(1-\phi)}\frac{\partial\phi}{\partial z}\right], \tag{17}$$

with boundary conditions

$$\phi(0) = \frac{\Phi^2}{\Phi+\mathcal{H}(1-\Phi)} \equiv \phi_0(\mathcal{H}), \quad \phi(l) = \Phi, \tag{18a,b}$$

and initial condition $\phi(t=0) = \Phi$. The functions $Q(t)$ and $l(t)$ satisfy

$$Q = \frac{-\Phi^2\phi_0}{(1-\Phi)(1-\phi_0)^2}\left.\frac{\partial\phi}{\partial z}\right|_0, \tag{19a}$$

$$\frac{\partial l}{\partial t} = Q + \frac{\Phi^3}{(1-\Phi)^3}\left.\frac{\partial\phi}{\partial z}\right|_l, \tag{19b}$$

with initial condition $l(t=0) = 1$.

### 2. Steady-state theory

In a steady state, the flux $Q_s$, depth of the medium $l_s$ and effective permeability $k_{\text{eff}}$ are given from (13) by

$$Q_s = -\frac{\Phi^2}{(1-\Phi)^2}\left\{\log\left[1+\frac{\mathcal{H}\Phi}{\Phi+\mathcal{H}(1-\Phi)}\right] - \frac{\mathcal{H}\Phi(1-\Phi)}{\Phi+\mathcal{H}(1-\Phi)}\right\}, \tag{20}$$

$$l_s = \frac{\Phi^2}{Q_s(1-\Phi)}\left\{\log\left[1+\frac{\mathcal{H}\Phi}{\Phi+\mathcal{H}(1-\Phi)}\right] - \frac{\mathcal{H}\Phi}{(\Phi+\mathcal{H})(1-\Phi)}\right\}, \tag{21}$$

$$k_{\text{eff}} = -\frac{Q_s l_s}{\mathcal{H}}, \tag{22}$$

while the porosity $\phi(z)$ is given implicitly from the integral of (8) by

$$\frac{\phi-\Phi}{(1-\phi)(1-\Phi)} + \log\left(\frac{1-\phi}{1-\Phi}\right) = \frac{(1-\Phi)Q_s l_s}{\Phi^2}\left(1-\frac{z}{l_s}\right). \tag{23}$$

If required, the displacement $\zeta(z)$ of the medium can be calculated from the integral of (23) using (3).

In the limit of large applied fluid pressure $\mathcal{H} \to \infty$,

$$Q_s \to \frac{\Phi^2}{(1-\Phi)^2}[\log(1-\Phi)+\Phi], \tag{24a}$$

$$l_s \to \frac{\Phi\log(1-\Phi)}{\log(1-\Phi)+\Phi} - 1, \quad k_{\text{eff}} \to 0. \tag{24b}$$

These results indicate that, given the constitutive relationships (15), both the flux and the depth of the medium tend towards finite values as the pressure difference diverges, in striking contrast to flow through a rigid medium where the flux increases linearly with the pressure difference.

### 3. Example results of the model

We solved (17) numerically using a second-order finite difference method and a semi-implicit time-stepping scheme. The length of the domain was scaled to unity by the introduction of a rescaled coordinate $y = z/l(t)$. At each time step, $Q(t)$ and $l(t)$ were determined from the boundary conditions (19).

Figure 2 shows how the flux, depth, and porosity evolve to the steady state following a step increase in the applied pressure $\mathcal{H}$ at $t = 0$. Initially, the porosity is uniform throughout the medium. As soon as fluid begins to flow, the medium compacts

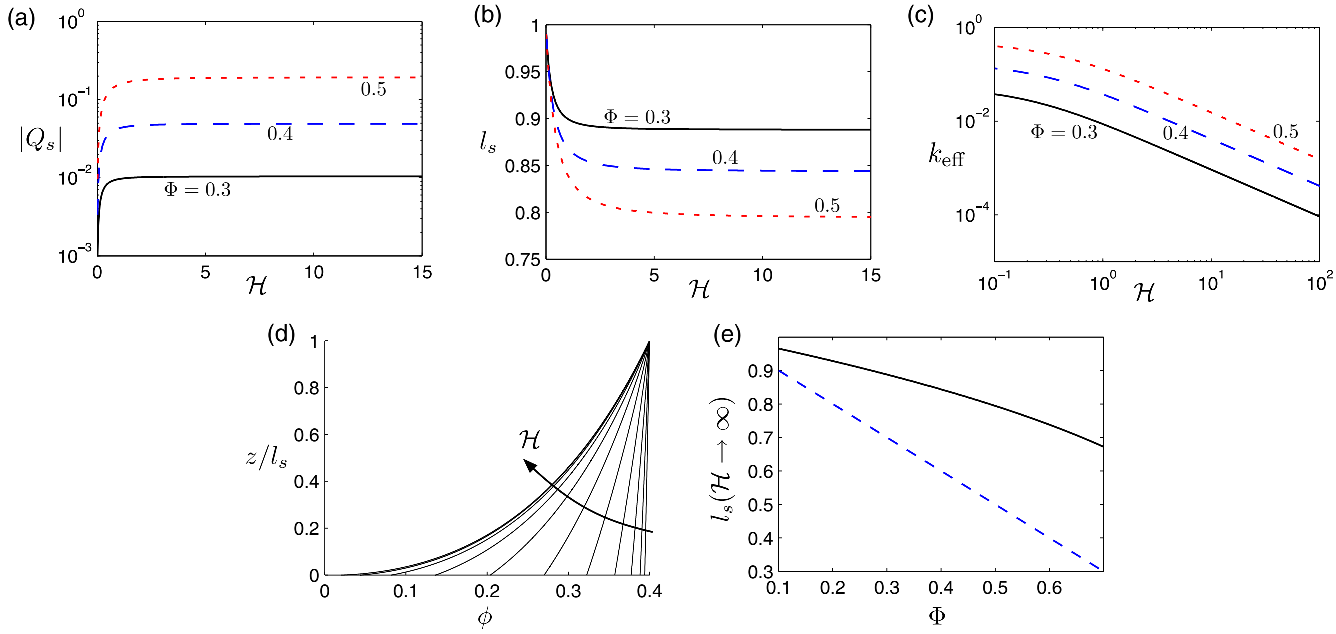

FIG. 3. Steady-state results of the specific model, for $\Phi = 0.3$ (black line), $\Phi = 0.4$ (blue long dashed), and $\Phi = 0.5$ (red short dashed): (a) the magnitude of the flux $Q_s$; (b) the depth $l_s$ of the medium; and (c) the effective permeability $k_{\rm eff}$ of the medium. (d) The porosity $\phi(z/l_s)$ for $\Phi = 0.4$ and different values of $\mathcal{H}$ between $\mathcal{H} = 0.01$ and $\mathcal{H} = 10.24$ separated by a factor of 2. (e) The asymptotic prediction for the minimum depth from (24b) (black solid), and the corresponding theoretical minimum value $l_s = 1 - \Phi$ for compression under an arbitrary external load (blue dashed).

instantaneously at the base to $\phi_0(\mathcal{H})$ given by (18a) [see Fig. 2(c)]. The resultant boundary-layer structure in the profile of $\phi(z)$ spreads as the porosity evolves towards a steady profile through the medium. Both the flux and the depth of the medium decrease over time and approach a steady value [Figs. 2(a) and 2(b)]. The time scale over which the medium adjusts does not appear to depend strongly on $\mathcal{H}$. The corresponding evolution of $\phi$ following a subsequent step decrease in $\mathcal{H}$ [Fig. 2(d)] is not a simple reversal of the behavior above. Instead, the porosity at the base instantly adopts a new higher value, while the differentially compacted medium above gradually decompacts over time.

Steady-state solutions (Fig. 3) confirm that, in the limit $\mathcal{H} \to \infty$, the flux and depth of the medium tend to finite values [cf. (24)] while the effective permeability decreases like $\mathcal{H}^{-1}$ (cf. (22)). The porosity also approaches an asymptotic profile with $\phi_0 \to 0$ as $\mathcal{H} \to \infty$. Unlike the transient evolution, the steady-state solutions are independent of whether $\mathcal{H}$ was increased or decreased to its final value.

An interesting comparison can be made between the maximum compaction of the medium for compression by an external load and compression driven by fluid flow. Based on conservation of solid, if the medium were compressed with arbitrary external load, the depth of the medium would tend towards $l_s \to 1 - \Phi$, which is significantly lower than the prediction for flow-induced compaction (24b) as shown in Fig. 3(e). External loading can achieve much greater compaction than pressure-driven flow because under an external load the entire medium compacts uniformly. In contrast, under pressure-driven flow the porosity at the upper surface is fixed at its initial value, because the matrix pressure vanishes and the matrix remains unstrained there.

## III. EXPERIMENTS

### A. Setup and experimental process

In this section we discuss a set of experiments in which we explored fluid-driven deformation of a simple, optically accessible poro-elastic medium. The experimental setup, shown in Fig. 4, consisted of a rectangular acrylic tank 25 cm tall, 12 cm across, and 2 cm deep. The tank contained small, roughly spherical, hydrogel particles, saturated with water. The particles were a sodium poly-acrylamide hydrogel (obtained

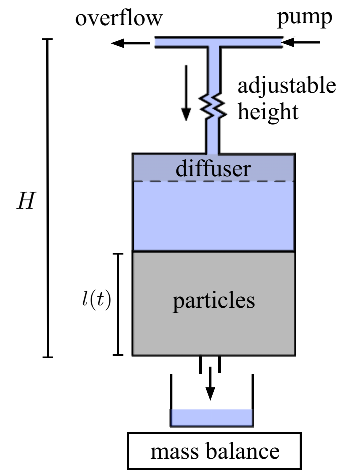

FIG. 4. A schematic showing the experimental setup, as described in the main text. The tee junction was connected to an adjustable clamp that could be moved up or down to set the desired pressure head $H$. Arrows show the direction of the flow when the exit valve at the base of the tank was opened.

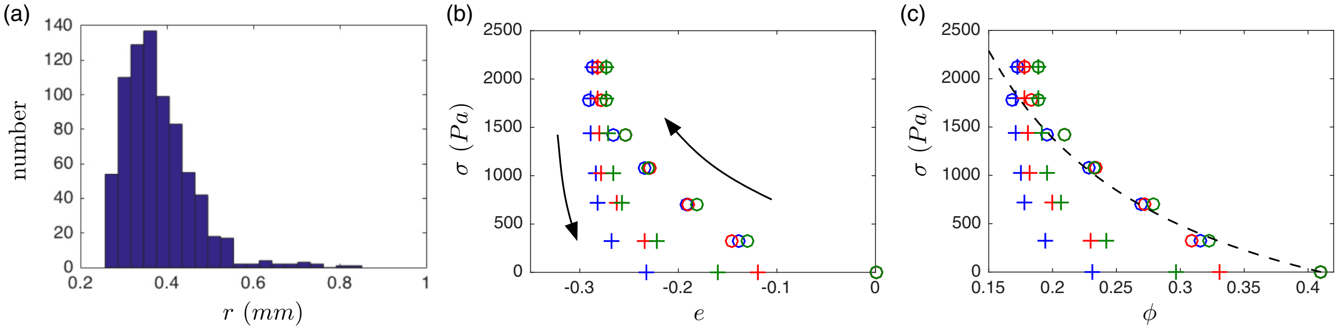

FIG. 5. Properties of the swollen beads. (a) Histogram of the radii of a sample of 763 particles, measured by image processing a photograph of a monolayer of saturated particles. The mean radius is 0.380 mm, which is used to estimate the Kozeny-Carman permeability scale $k^* = r^2/45 = 3.2 \times 10^{-9}$ m$^2$, and the standard deviation is 0.08 mm. (b) Stress $\sigma$ as a function of strain $e$, measured as described in the main text from tests in which the stress was increased and then decreased as indicated by the arrows. The measurements for increasing stress (circles) deviate appreciably from those for decreasing stress (crosses). The same test was repeated three times, shown as blue, red, and green, consecutively. (c) The same data as in (b), converted into a function of $\phi$ using (2), with $\Phi = 0.41$. The data for increasing stress are compared to a simple fit of the form (15a) with an elastic modulus of $\sigma^* = 1900$ Pa (dashed).

from JRM Chemical) that, when saturated, had a radius of $0.38 \pm 0.16$ mm [Fig. 5(a)] and a density and refractive index that was very close to water. In order to measure deformation of the medium, tracer hydrogel particles were added to the mixture; we had previously treated these particles with a solution of $CuSO_4$ which made them green [26].

At the base of the tank there was a metal grill lined with permeable fabric, through which particles could not pass but through which water could flow, and an exit valve that could be opened to the atmosphere. At the top of the tank, water could enter through a flexible tube and across a sponge diffuser. The flexible tube was 1.5 m long and connected to a tee junction; one end of the junction was fed continuously by a peristaltic pump and the other was open to the atmosphere and allowed to overflow. The junction could be moved up and down vertically next to the tank to set the desired pressure head $H$. Once secured at this height, the exit valve on the tank was opened, fluid flowed through the medium, and the coupled pump and open tube ensured that the depth of the water remained fixed at the height of the junction. The experimental setup allowed for the tee junction to be lowered to heights below the top of the particles while the particles remained fully saturated. The pressure head could therefore be set at values $H < l_0$, and lowered as far as $H = 0$.

For each experiment, at each pressure head (accurate to 0.5 cm) the fluid flux per unit cross-sectional area through the medium was measured using a standard digital mass balance (accurate to 0.01 g), and the depth of the medium was measured by interface tracking from photographs, taken using a standard digital SLR camera. The deformation of the medium was measured using image-analysis software [27] to detect and track the displacement of tracer particles in the matrix (accurate to the order of the diameter of the particles, ~0.8 mm).

The experimental procedure involved taking measurements at sequentially increasing values of $H$ at 10 cm intervals between 0 cm and 120 cm, followed by sequentially decreasing values back down to $H = 0$ cm. This sweep of increasing and decreasing applied pressure was repeated four times. At each value of $H$ the system was left for 30 seconds to attain an apparently steady state before the measurements of flux, depth, and displacement were taken. Although the main aim of this study was to investigate the steady-state behavior, in some experiments the flux was also measured over time as the system evolved to the steady state.

### B. Rheology

The main source of uncertainty for a quantitative comparison of the experiments and the theoretical model is the porosity $\Phi$ of the unstressed medium. Hydrogel spheres are microporous particles composed mainly of water, which makes accurate measurement of porosity extremely difficult. Based on a rough comparison with measurements from a sample of loose, random-packed, similar-sized glass spheres, we used a value of $\Phi = 0.41$ for all the experimental comparisons presented here.

The approximate rheology of the saturated deformable medium was measured by simple unidirectional compression tests. The same rectangular acrylic cell was fitted with an impermeable base, filled with saturated hydrogel particles, and overlain by a removable porous piston. Weights were added to or removed from the piston to exert a known downwards force on the medium. Since the density of fluid and solid were approximately equal, there was very little differential compaction of the medium under gravity in this setup, and the porosity was assumed to be vertically uniform. Experiments were conducted by sequentially increasing and then decreasing the load on the piston and measuring its vertical displacement $\Delta l$ away from the initial depth $l_0$ at each load, thereby giving the macroscopic strain $e \equiv \Delta l / l_0$ of the medium.

Measurements of $\sigma(e)$ [Fig. 5(b)] from three sets of experiments are converted into functions of the porosity using (2) with $\Phi = 0.41$, as shown in Fig. 5(c). In each set of experiments, there is a clear hysteresis between increasing and decreasing stress, which we will revisit in Sec. III C. The results for increasing stress are relatively well fitted by the simple model constitutive equation (15) with a modulus of $\sigma^* = 1900$ Pa.

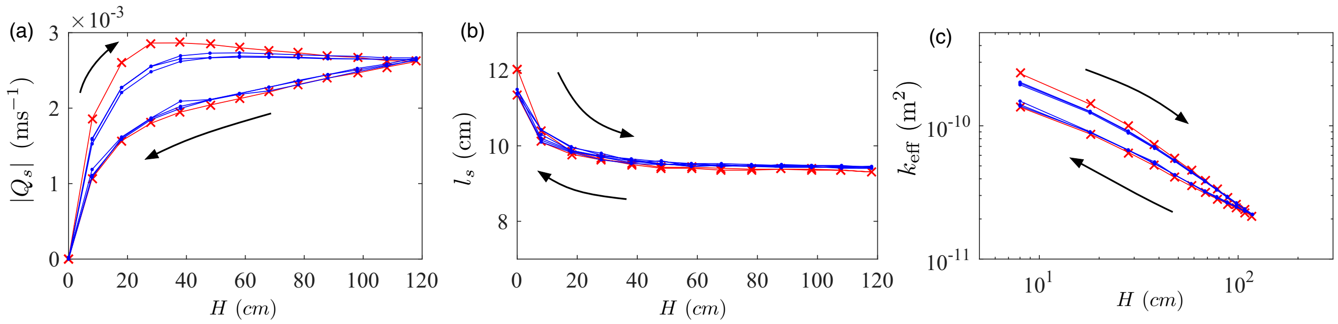

FIG. 6. Experimental results with $l_0 = 11.4$ cm for a series of experiments in which the height $H$ was increased and then decreased four times. (a) The flux per unit cross-sectional area $Q_s$, (b) the depth $l_s$, and (c) the effective permeability $k_{\rm eff}$. The first sweep up and down in shown in red with crosses. Arrows show the direction of increasing and decreasing $H$. After the first sweep, the measurements of the flux and the effective permeability collapse onto reproducible hysteresis loops.

Note, however, that the stress increases more steeply than the model predicts at the lowest porosities [Fig. 5(c)]. Equivalently, the limiting macroscopic strain $e_m$ appears (by extrapolation of the trend in [Fig. 5(b)] to be rather smaller in magnitude than the model prediction of $e_m = -\Phi = -0.41$. These discrepancies may be a result of the simplifying assumption of a zero minimum porosity $\phi_m$ in the model, and perhaps suggest that $\phi_m > 0$ for these hydrogel particles. Of course, the true rheology of hydrogel particles under large stress is rather complex. For example, it seems plausible that the particles might deform so as to seal off connected passages through the medium and become essentially impermeable, and thus incompressible, at a nonzero porosity. On the other hand, swollen gels can release a fraction of their internal fluid under pressure [28], which would result in higher porosities than the measurements indicate. Previous measurements [28] suggest a loss of volume of less than 10% at the pressures achieved in these experiments. Despite these various uncertainties, given the reasonable agreement in Fig. 5(c), we retain the simple model rheology with $\phi_m = 0$ for all the comparisons in this section.

### C. Experimental results

Note that all the variables referred to in this section are dimensional.

Steady-state measurements from a full set of four increasing and decreasing sweeps of the applied pressure (Fig. 6) reveal a number of notable features. First, measurements of $Q_s$ and $k_{\rm eff}$ display a clear hysteresis between increasing and decreasing stress. Both measures are significantly lower when the stress is decreased compared to when it is increased. Although hysteresis is less clear in the measurements of $l_s$, close examination suggests it is still present, with the depth being lower when $H$ is decreased. Second, with the exception of the first sweep of increasing and decreasing $H$, the hysteresis loop appears to be reproducible. The slight difference in the first sweep was observed in all sets of results, and is likely indicative of some mechanical rearrangement of the particles as the stress on the medium is first increased. In particular, after the first sweep the depth of the medium $l_s$ reproducibly returns to a value at $H = 0$ that is lower than its initial value. Third, the flux and the depth of the medium both appear to saturate towards a plateau as the stress is increased, while the effective permeability continually decreases, much as in the results of the theoretical model [Figs. 2(d) and 2(e)].

Measurements from three sets of experiments for different initial depths $l_0$ all exhibit the same features as just discussed, and, after suitable nondimensionalization, agree relatively well between themselves (Fig. 7). The slight difference in the magnitude of the dimensionless flux as $\mathcal{H} \to \infty$ [Fig. 7(a)]

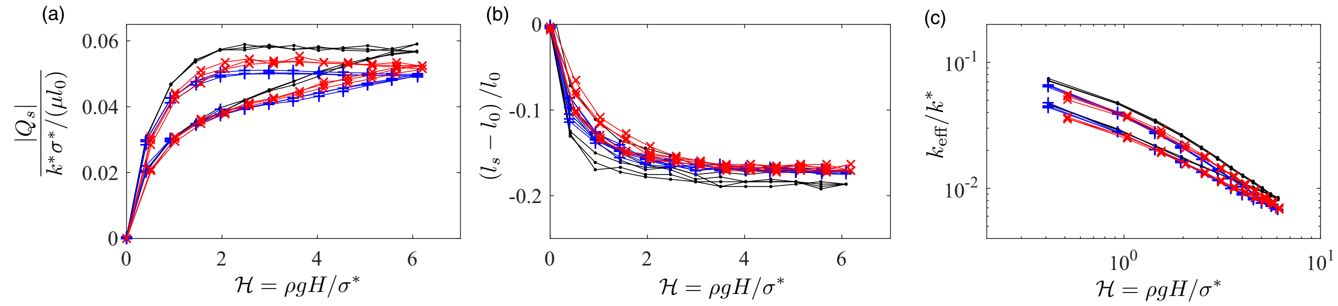

FIG. 7. Experimental results for three sweeps of increasing and decreasing $H$, scaled by the dimensional scalings of §II, for $l_0 = 8.9$ cm (black dots), 11.4 cm (blue pluses), and 13.3 cm (red crosses). (a) The dimensionless flux $Q_s \mu l_0/k^*\sigma^*$, (b) the dimensionless change in the depth $(l_s - l_0)/l_0$, and (c) the dimensionless effective permeability $k_{\rm eff}/k^*$. Note that all results are taken after one initial sweep of increasing and decreasing $H$, and $l_0$ was chosen to be the height of the medium after this sweep, rather than the initial height, in an attempt to account for any particle rearrangement (and thus changing of $\Phi$) during the initial sweep. The other parameters were $\sigma^* = 1900$ Pa, $\Phi = 0.41$, $\rho = 1000$ kg m$^{-3}$, a measured viscosity of $\mu = 9.336 \times 10^{-4}$ Pa s, and $k^* = r^2/45 = 3.2 \times 10^{-9}$ m$^2$.

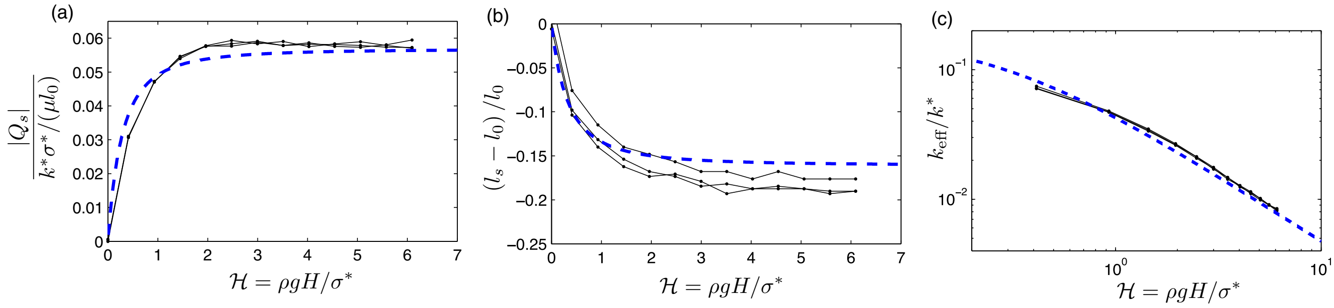

FIG. 8. Comparison of the experimental results from three sweeps as in Fig. 7, showing only the measurements for increasing $H$ (black), with the predictions of the theoretical model (blue dashed), for experiments with $l_0 = 8.9$ cm. The other parameters are as in Fig. 7.

is perhaps due to a slightly different initial porosity $\Phi$ between the different experiments.

Explicit comparison of the steady-state experimental results and the predictions of the theoretical model shows good agreement for the increasing branch of the hysteresis loop (Fig. 8). Both theory and experiment show that the magnitude of the flux $Q_s$ increases steeply from zero as $H$ is increased, and tends towards a finite plateau for large $H$. The effective permeability decreases correspondingly, while the depth $l_s$ of the medium also decreases towards an asymptotic value. The theoretical prediction of $l_s$ appears to be slightly high, although the general trend with $H$ agrees with the experimental data. The theory differs significantly from the measurements for the decreasing branch of the hysteresis loop. This difference is not surprising given the significant difference in the rheology of the particles for increasing or decreasing stress (Fig. 5), which is not included in the model.

In order to quantify the degree of internal deformation, we measured the displacement of the medium as a function of depth by tracking a number of dyed particles over the course of multiple sets of experiments for increasing and decreasing stress. The results are shown in Fig. 9. The displacements for increasing stress roughly collapse when the measurements are scaled by $l_0$ [Fig. 9(a)]. As the height $H$ of water is increased, the displacement of the particles increases. For all values of $H$, the displacement field is nonlinear in the vertical coordinate, which indicates that the medium compacts differentially, as predicted by the model. This feature is more clearly observed in Fig. 9(b), which shows smoothed profiles of the measurements from increasing and decreasing sweeps of $H$. This figure also shows that the deformation for large $H$ becomes insensitive to changes in $H$, as suggested by the limiting behavior of $l$: the profiles for $H = 80$ cm and $H = 120$ cm are almost indistinguishable.

Predictions of the model, also shown in Fig. 9(a), give qualitatively similar profiles to the measured displacement fields. The theory gives a fairly accurate quantitative prediction of the measured displacement for large $H$, but appears to overpredict the extent of deformation for small $H$, which is interesting given the good agreement between the measurements in Fig. 8. The theoretical curves reach the upper surface with an infinite slope, which corresponds to a vanishing strain, and thus a

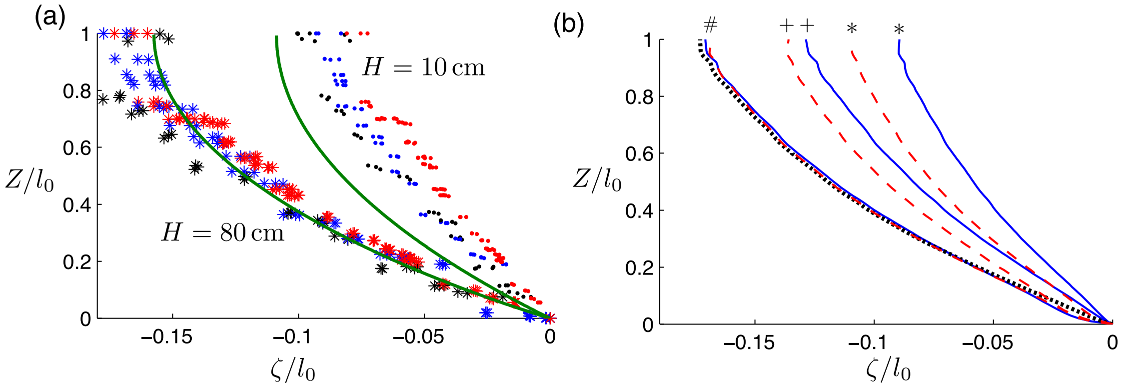

FIG. 9. Measurements from particle tracking of the dimensionless displacement $\zeta/l_0$. For a particle at depth $z$, the displacement is defined by the vertical distance traveled relative to its initial position $Z$, such that $\zeta = z - Z$. Measurements are shown as a function of the dimensionless initial (Lagrangian) position $Z/l_0$, for different initial depths $l_0 = 8.9$ cm (black), 11.4 cm (blue), and 13.3 cm (red). Each experiment comprised three sweeps of increasing and decreasing $H$, and the displacement in each case was measured relative to the position of the particles at the start of that sweep. All measurements were taken after one initial sweep of increasing and decreasing stress, to allow for any initial rearrangement of particles. (a) Measurements for increasing $H$ at $H = 10$ cm (dots) and $H = 80$ cm (stars), together with predictions of the theoretical model (green lines) given by (3) and (23) using the parameters as in Fig. 7. (b) Smoothed profiles of the experimental measurements for $l_0 = 11.4$ cm, for increasing stress (blue solid) and decreasing stress (red dashed) at $H = 10$ cm (indicated by a star), $H = 20$ cm (indicated by a cross), $H = 80$ cm (indicated by #), and $H = 120$, which was the highest stress reached (black dotted).

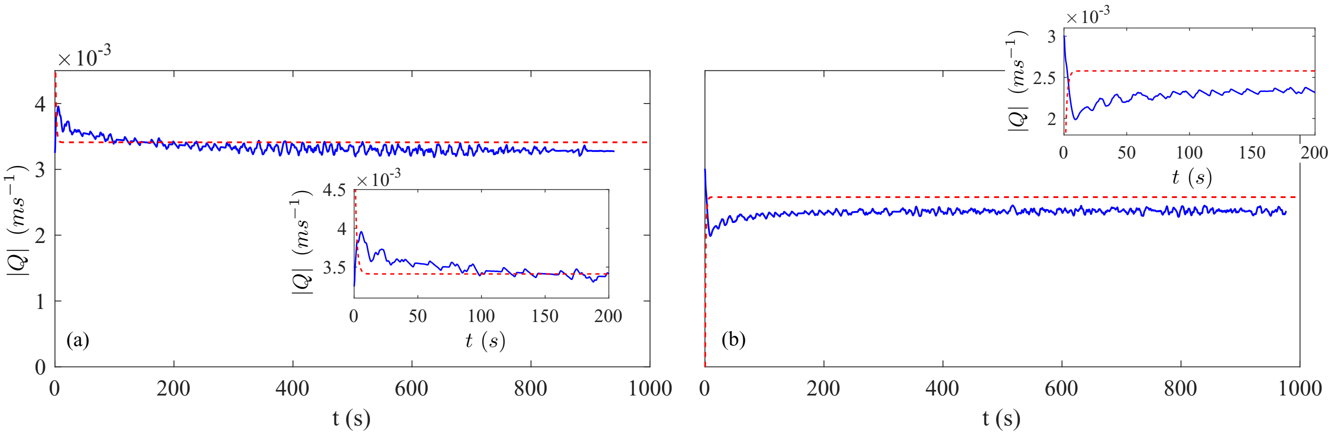

FIG. 10. Smoothed measurements of the flux over time for a set of experiments with $l_0 = 13.3$ cm, following a step change in the height at $t = 0$: (a) from $H = 10$ cm up to $H = 40$ cm, and (b) from $H = 130$ cm down to $H = 40$ cm. The red dashed lines show the predicted flux using the time-dependent model, with the parameters as in Fig. 7. The insets show the comparisons at early times in more detail. It is evident that the experiment evolves over a much longer time scale than the theory predicts.

uniform porosity $\Phi$, there. The resolution of the measurements near the upper surface is not sufficient to determine whether they agree with this behavior, although the slopes of the profiles in Fig. 9(b) appear to be increasing towards vertical in agreement with theory.

Given the hysteretic behavior shown in Fig. 6, it is not surprising that the measurements for increasing and decreasing stress give different displacement profiles [Fig. 9(b)]. The magnitude of the displacement remains larger through the medium for decreasing stress than for increasing stress, which indicates that the average porosity is lower. This observation is consistent with the previous observations of a lower flux and depth for decreasing stress. Interestingly, the displacement becomes very similar between increasing and decreasing stress for higher values of $H$ [e.g., the comparison at $H = 80$ cm in Fig. 9(b)], even though previous measurements indicate that the flux might differ appreciably [Fig, 6(a)]. In other words, small variations in the vertical structure of the medium can have a relatively large effect on the macroscopic properties when the pressure head is large, or, alternatively, when the porosity is small at the base of the medium.

Finally, we comment briefly on some experiments in which the evolution of the flux was measured over time following a change in $H$. Figure 10 shows measurements of the flux $Q$ over time as the pressure head was first increased and then decreased, together with the predictions of the model. The comparison shows that the flux evolves over a much longer time scale than the model predicts. The poro-elastic time scale of the model is based on the assumptions of a bulk elastic rheology for the matrix and a constant composition and mass of each phase during compression. However, given that each hydrogel particle is predominantly made up of fluid, there may also be a pore-scale viscous contribution to the stress (i.e., a strain-rate dependence), which could introduce an additional, visco-elastic, time scale. For example, in the experiments fluid may be seeping out of the swollen hydrogels as they deform under compression, which is a viscous process that is not included in the model. Previous experiments of injection-driven deformation using similar hydrogel particles have also suggested the presence of a viscous-compaction time scale [17]. More generally, visco-elastic behavior has been widely observed in suspensions of hard colloidal particles or emulsions (e.g., Refs. [29–31]), but under conditions of shear rather than compression.

Note that, as well as highlighting a difference in times cales, the comparison in Fig. 10 also indicates clearly the hysteresis in the measurements of $Q$, which is absent from the model.

## IV. DISCUSSION AND CONCLUSIONS

In this paper we have presented experimental and theoretical models to describe flow-induced one-dimensional compaction of a deformable medium. The experimental setup consisted of a porous matrix comprising small deformable hydrogel spheres in a rectangular cell, through which water was driven by an applied pressure difference that could be varied. The flux of fluid, bulk deformation, and internal deformation were all measured as functions of pressure difference. While the experimental setup utilised gravity to drive flow, the results apply to any pressure-driven flow because the fluid and solid densities were matched.

In a classical rigid medium, the fluid flux increases linearly with the applied pressure. Perhaps the most striking result of this work is that if the medium is deformable, this may not be the case. Instead, the flux can increase towards a finite maximum as the pressure is increased, as we observed experimentally. The depth of the medium correspondingly decreases towards a finite asymptotic value, and, as a consequence, the "effective permeability" of the medium, defined in terms of the bulk pressure drop and fluid flux, decreases towards zero. Thus, quite counterintuitively, the flux through a deformable medium can become insensitive to the applied fluid pressure difference for large pressures: the flow is self-regulated by the medium, as increased pressure gradients balance increased resistance from the permeability.

For all of this behavior, we found good quantitative agreement between our experiments and our theoretical model when the applied pressure difference was sequentially increased. In particular, the dimensional analysis underlying the scalings of the model indicates that the steady-state flux per unit area, depth of the medium, and effective permeability are

$$Q_s = -\frac{k^*\sigma^*}{\mu l_0} f_1; \quad l_s = l_0 f_2/f_1; \quad k_{\text{eff}} = \frac{k^*\sigma^*}{\rho g H} f_2, \tag{25a,b,c}$$

respectively, for some dimensionless functions $f_1(\Phi,\mathcal{H} \equiv \rho g H/\sigma^*)$ and $f_2(\Phi,\mathcal{H})$. For the simple elastic rheology considered in this paper, these functions are given by (20) and (21), respectively. More generally, the factors that control whether or not these functions, and thus the flux, tend to a finite value, as in this paper, or increase without bound, as in a rigid medium, are dictated by the appropriate constitutive laws for the material, as discussed in the Appendix.

From a practical point of view, one might be interested in maximizing the fluid flux through the medium. If the flux tends to a finite value as the pressure drop is increased, it can become extremely inefficient to increase the pressure drop beyond a certain value. For example, based on the results of the theoretical model (Fig. 3), the steady-state flux is within 5% of its asymptotic value once the pressure drop $\rho g H$ is approximately double the elastic modulus $\sigma^*$ of the medium (i.e., $\mathcal{H} \approx 2$); thus an increase in the applied pressure beyond this value causes only a very small change in the flux.

A key difference between compression driven by an external load or by fluid flow is that, in the latter case, the requisite gradient in the fluid pressure induces a gradient in the matrix stress, which corresponds to a gradient in the porosity. By direct measurement of the displacement field through the solid medium, we confirmed this behavior experimentally. As a consequence of differential compaction, an applied fluid pressure drop will result in appreciably less overall compaction than the same pressure applied as an external load, as demonstrated in Fig. 3(e).

There are two significant discrepancies between the experimental observations and the theoretical model. The first is the presence of hysteresis in the experimental measurements: the steady state of the system has a strong dependence on the previous stress state, or previous degree of compaction. Repeatable hysteresis was observed in all the measurements, including in the detailed deformation of the medium. The extent to which such hysteresis is a particular feature of this experimental material is not clear. It does, however, seem plausible that any collection of deformable particles could rearrange under stress into a new configuration from which they could not simply revert on the relaxation of that stress (cf. "jamming" in hard granular media: see, e.g., Ref. [32]). Indeed, this effect might be heightened if fluid were also released from the particles under stress, reducing the particle volume and allowing for further rearrangement.

The second discrepancy is that the theory significantly underpredicts the time scale of evolution to a new steady state following a step change in the applied pressure, as discussed at the end of Sec. III C. The transient evolution of the system was not the main focus of this work, and warrants further study.

## ACKNOWLEDGMENTS

D.R.H. was supported by a Killam Postdoctoral Fellowship and a Research Fellowship at Gonville and Caius College, Cambridge. During the experimental part of this project, J.S.N. was supported by the division of Engineering Science, University of Toronto. J.A.N. is partly supported by a Royal Society University Research Fellowship.

## APPENDIX : IMPLICATIONS OF THE THEORETICAL MODEL IN THE LIMIT OF LARGE APPLIED FLUID PRESSURE $\mathcal{H} \to \infty$: IS THE FLUX BOUNDED?

In the experiments and the specific model considered in this paper, the magnitude of the steady-state flux $Q_s$ tends towards a finite value as $\mathcal{H} \to \infty$. It is not obvious, *a priori*, whether such behavior is a generic feature of the model framework irrespective of the choice of solid rheology $\sigma(e(\phi))$ or permeability $k(\phi)$. Indeed, one could envision three plausible scenarios in general: the strength of the flow could continually increase as the pressure drop increases (as in a rigid medium); the flow could tend towards a finite value (as in the experiments); or the strength of the flow could decrease as the overpressure compresses the medium and reduces the permeability.

The steady-state solutions of the general theoretical framework outlined in Sec. II A can be analyzed to determine the generic behavior $Q_s$ as $\mathcal{H} \to \infty$ for any function $\sigma(\phi)$ and any non-negative $k(\phi)$. From (13a),

$$\frac{\partial Q_s}{\partial \mathcal{H}} = -\frac{(1-\phi_0)k(\phi_0)\sigma'(\phi_0)}{(1-\Phi)}\frac{\partial \phi_0}{\partial \mathcal{H}}, \tag{A1}$$

where the porosity $\phi_0$ at the base is determined by the boundary condition $\sigma(\phi_0) = \mathcal{H}$, or, after differentiation, $\sigma'(\phi_0)\partial\phi_0/\partial\mathcal{H} = 1$. Thus, (A1) reduces to

$$(1-\Phi)\frac{\partial Q_s}{\partial \mathcal{H}} = -(1-\phi_0)k(\phi_0) \tag{A2}$$

(recall that $Q_s$ is negative), which indicates that $\partial Q_s/\partial\mathcal{H}$ is always negative. The flow therefore cannot weaken as $\mathcal{H}$ is increased, and the third hypothesis described above is not possible within this model framework.

In general, we would expect the stress to diverge and the permeability to vanish as the porosity approaches some minimum value $\phi_m$ (in the specific model of this paper, $\phi_m = 0$). Suppose, in the limit $\phi \to \phi_m$, $k \sim (\phi - \phi_m)^\alpha$ and $\sigma \sim (\phi - \phi_m)^{-\beta}$, for some positive constants $\alpha$ and $\beta$. Then $\phi_0 - \phi_m \sim \mathcal{H}^{-1/\beta}$ and (A2) gives

$$\frac{\partial Q_s}{\partial \mathcal{H}} \sim -\mathcal{H}^{-\alpha/\beta} \quad \text{as} \quad \mathcal{H} \to \infty. \tag{A3}$$

If $\alpha > \beta$, then $Q_s \sim$ constant as $\mathcal{H} \to \infty$ and the flux tends to a finite value as the pressure head is increased. If instead $\alpha = \beta$ or $\alpha < \beta$, then $Q_s \sim \log\mathcal{H}$ or $Q_s \sim O(\mathcal{H}^{(\beta-\alpha)/\beta})$, respectively, and the flux continues to increase as the pressure head is increased. In the specific model outlined in Sec. II B, $\alpha = 3$ and $\beta = 1$ such that $\alpha > \beta$, and so the flux tends to a constant for large $\mathcal{H}$.

Physically these two scenarios describe a different balance as the stress on the medium diverges. In the former case, the increased fluid pressure balances the increased resistance to flow from the permeability such that the flux is constant as the pressure increases. In the latter case, the matrix is sufficiently strain hardening that it is able to absorb the increase in the fluid pressure without restrictively blocking the pathways to fluid flow, and the flux increases without bound, as in a rigid medium.

[1] O. Coussy, *Poromechanics* (Wiley, New York, 2004).

[2] E. Detournay and A. H.-D. Cheng, *Comprehensive Rock Engineering: Principles, Practice and Projects, vol II, Analysis and Design Method* (Pergamon Press, Oxford, 1993), Chap. 5, pp. 113–171.

[3] J. E. Elkhoury, E. E. Brodsky, and D. C. Agnew, Seismic waves increase permeability, Nature (London) **441**, 1135 (2006).

[4] Z. Shi, G. Wang, M. Manga, and C.-Y. Wang, Continental-scale water-level response to a large earthquake, Geofluids **15**, 310 (2015).

[5] M. Manga and E. Brodsky, Seismic triggering of eruptions in the far field: volcanoes and geysers, Annu. Rev. Earth Planet Sci. **34**, 263 (2006).

[6] D. M. Audet and A. C. Fowler, A mathematical model for compaction in sedimentary basins, Geophys. J. Int. **110**, 577 (1992).

[7] A. C. Fowler and X. S. Yang, Fast and slow compaction in sedimentary basins, SIAM J. Appl. Math. **59**, 365 (1998).

[8] R. G. de Kretser, P. J. Scales, and D. V. Boger, Improving clay-based tailings disposal: case study on coal tailings, AIChE J. **43**, 1894 (1997).

[9] D. J. Lee and C. H. Wang, Theories of cake filtration and consolidation and implications to sludge dewatering, Water Resour. Res. **34**, 1 (2000).

[10] M. A. Hubbe and J. A. Heitmann, Review of factors affecting the release of water from cellulosic fibers during paper manufacture, BioResources **2**, 500 (2007).

[11] R. G. Lentle, P. W. M. Janssen, and I. D. Hume, The roles of filtration and expression in the processing of digesta with high solid phase content, Comp. Biochem. Physiol. **154**, 1 (2009).

[12] R. Burger, F. Concha, and F. M. Tiller, Application of the phenomenological theory to several published experimental cases of sedimentation processes, Chem. Eng. J. **80**, 105 (2000).

[13] R. G. de Kretser, D. V. Boger, and P. J. Scales, Compressive rheology: an overview, Rheol. Rev. 125 (2003).

[14] A. D. Stickland and R. Buscall, Whither compressional rheology?, J. Non-Newtonian Fluid Mech. **157**, 151 (2009).

[15] K. H. Parker, R. V. Mehta, and C. G. Caro, Steady flow in porous, elastically deformable materials, J. Appl. Mech. **54**, 794 (1987).

[16] Y. Lanir, S. Sauob, and P. Maretsky, Nonlinear finite deformation response of open cell polyurethane sponge to fluid filtration, J. Appl. Mech. **57**, 449 (1990).

[17] C. W. MacMinn, E. R. Dufresne, and J. S. Wettlaufer, Fluid-Driven Deformation of a Soft Granular Material, Phys. Rev. X **5**, 011020 (2015).

[18] K. N. Nordstrom, E. Verneuil, W. G. Ellenbroek, T. C. Lubensky, J. P. Gollub, and D. J. Durian, Centrifugal compression of soft particle packings: Theory and experiment, Phys. Rev. E **82**, 041403 (2010).

[19] D. R. Hewitt, J. A. Neufeld, and N. J. Balmforth, Shallow, gravity-driven flow in a poro-elastic layer, J. Fluid Mech. **778**, 335 (2015).

[20] D. A. Drew, Mathematical modeling of two-phase flow, Ann. Rev. Fluid Mech. **15**, 261 (1983).

[21] R. Buscall and L. R. White, The consolidation of concentration suspensions, J. Chem. Soc., Farady Trans. 1 **83**, 873 (1987).

[22] K. A. Landman, L. R. White, and M. Eberl, Pressure filtration of flocculated suspensions, AIChE Journal **41**, 1687 (1995).

[23] J. R. Philip and D. E. Smiles, Macroscopic analysis of the behaviour of colloidal suspensions, Advances in Colloid and Interface Science **17**, 83 (1982).

[24] C. W. MacMinn, E. R. Dufresne, and J. S. Wettlaufer, Large deformations of a soft porous material (unpublished).

[25] S. S. L. Peppin, J. A. W. Elliot, and M. G. Worster, Pressure and relative motion in colloidal suspensions, Phys. Fluids **17**, 053301 (2005).

[26] Z. F. Zoolshoev, S. A. Vesnebolotskaya, N. G. Bel'nikevich, and G. K. Elyashevich, Behavior of sodium polyacrylate hydrogels in copper sulfate solutions, Russian J. App. Chem. **81**, 1573 (2008).

[27] http://site.physics.georgetown.edu/matlab/.

[28] S. Vervoort, S. Patlazhan, J. Weyts, and T. Budtova, Solvent release from highly swollen gels under compression, Polymer **46**, 121 (2005).

[29] T. G. Mason, J. Bibette, and D. A. Weitz, Elasticity of Compressed Emulsions, Phys. Rev. Lett. **75**, 2051 (1995).

[30] I. Sumita and M. Manga, Suspension rheology under oscillatory shear and its geophysical implications, Earth Planet. Sci. Lett. **269**, 468 (2008).

[31] V. Trappe and D. A. Weitz, Scaling of the Viscoelasticity of Weakly Attractive Particles, Phys. Rev. Lett. **85**, 449 (2000).

[32] E. I. Corwin, H. M. Jaeger, and S. R. Nagel, Structural signature of jamming in granular media, Nature (London) **435**, 1075 (2005).